



Graphene quantum dots mediated charge transfer of CdSe nanocrystals for enhancing photoelectrochemical hydrogen production

Kai-An Tsai, Yung-Jung Hsu*

Department of Materials Science and Engineering, National Chiao Tung University, 1001 University Road, Hsinchu, Taiwan 30010, ROC



ARTICLE INFO

Article history:

Received 10 July 2014

Received in revised form

10 September 2014

Accepted 15 September 2014

Available online 22 September 2014

Keywords:

Graphene quantum dots

CdSe

Type-II band offset

Photoelectrochemical cells

Photocorrosion

ABSTRACT

We demonstrated the use of CdSe/graphene quantum dot (QD) nanoheterostructures as the photoanode for remarkable photoelectrochemical hydrogen production. By employing a delicate hydrothermal cutting approach, reduced graphene oxide (RGO) sheets with the lateral size in a desirable range can be obtained, from micrometer size (micro-RGO), to 30–100 nm (nano-RGO), and to 2–4 nm (QD-RGO). Because of the significant zigzag edge effect, nano-RGO and QD-RGO possessed well-defined band structure which enabled efficient light absorption and distinctive photoluminescence emission. Time-resolved photoluminescence spectra showed that nano-RGO and QD-RGO surpassed micro-RGO in enhancing the charge separation efficiency of CdSe. According to the cyclic voltammetry data, a type-II vectorial charge transfer model was considered for CdSe/nano-RGO and CdSe/QD-RGO nanoheterostructures, fundamentally different from the unidirectional electron transfer mechanism of CdSe/micro-RGO. Among the three CdSe/RGO samples tested, CdSe/QD-RGO achieved the highest photocurrent generation in the photoelectrochemical cell, which exceeded 5 times the value of CdSe. The incident photon-to-electron conversion efficiency (IPCE) spectra suggested that the significantly enhanced photoactivity of CdSe/QD-RGO originated from the type-II vectorial charge transfer feature, which not only promoted charge carrier separation but also improved the overall light harvesting. Furthermore, no appreciable decay of photocurrent was found for CdSe/QD-RGO after continuously used in the photoelectrochemical cell for over 2 h, revealing its substantially high stability during the water reduction process. The demonstrations from this work may facilitate the use of graphene QDs in semiconductor-based photocatalysis, in which the efficient light harvesting and high chemical inertness of graphene QDs can be well employed.

© 2014 Elsevier B.V. All rights reserved.

1. Introduction

Graphene, a two-dimensional (2D) single sheet of sp^2 -bonded carbon atoms, has spurred immense scientific interest since it became experimentally accessible in 2004 [1–3]. Because of the 2D atomic layer feature and unique electronic band structure, graphene exhibits many intriguing properties that make it a good candidate for potential applications in a wide array of fields, which include electronics, photonics, mechanics and materials chemistry [4–8]. Of particular importance is the use of graphene sheets in semiconductor-based photocatalytic applications. Recent developments have demonstrated the remarkable photocatalytic properties for semiconductor/graphene

nanoheterostructures [9,10]. Due to the high electrical conductivity, graphene sheets may serve as an effective electron acceptor for semiconductor nanostructures, which promotes charge carrier separation to enhance the photocatalytic efficiency. Besides, the high surface area of graphene sheets can increase the contact between the photocatalyst and reaction species, which is also conducive to improving the overall photocatalytic performance. Until now, various types of semiconductor/graphene nanoheterostructures have been proposed and investigated to facilitate further research and advancement [11–15]. In addition to photocatalysis, nanoheterostructures comprising graphene also find potential use for efficient energy conversion and storage, such as electrochemical cells, supercapacitors, photovoltaics and light emitting diodes [16].

Pristine graphene is a zero-gap material which behaves as a semi-metal with the massless Dirac fermions [17,18]. To diversify the electronic and optical applications, considerable efforts

* Corresponding author. Tel.: +886 3 5712121x55317; fax: +886 3 5724727.

E-mail addresses: yhsu@cc.nctu.edu.tw, yhsu@mail.nctu.edu.tw (Y.-J. Hsu).

to open up the bandgap of graphene are being pursued. Chemical modifications such as covalent functionalization and molecular doping have proven effective in modifying the electronic properties of graphene from near metallic to semiconducting [19–21]. For example, n-type electronic doping for graphene can be achieved via an appropriate covalent functionalization with nitrogen species [20]. This achievement affords the successful fabrication of n-type graphene field-effect transistors that can operate at room temperature. On the other hand, structural engineering that leads to quantum confinement, lattice perturbations, or edge effects also endows graphene with an energy gap [22–25]. In this regard, graphene structures with the lateral dimensions down to a few nanometers are particularly appealing because bandgap tailoring is made possible by controlling the characteristic size of the ultra-small graphene. As a representative example, graphene quantum dots (QDs) with a typical lateral size of 3–20 nm have emerged as a promising modified version of graphene. They possess many favorable attributes, such as tunable bandgap, large optical absorptivity, high photostability, good biocompatibility and fine dispersity in common solvents, which may push forward their practical applications in technologically important fields [26–33]. Especially, the calculated energy levels of graphene QDs suggest the capability of efficient light harvesting as well as the possibility of electron injection from graphene QDs to semiconductor [32,34], which shall stimulate further interest to combine graphene QDs and semiconductor nanostructures for photocatalysis applications, although it has not been well addressed thus far [35,36].

In this work, we investigated the photocatalytic properties of semiconductor/graphene QD nanoheterostructures for photoelectrochemical hydrogen production. The heterostructure samples were prepared by linking CdSe nanocrystals to graphene QDs using chitosan as the linker molecule [37]. Here, graphene QDs were obtained with the hydrothermal cutting approach [38], which involved the breaking of micrometer-sized reduced graphene oxide (RGO) sheets into nanometer-sized RGO pieces in the hydrothermal process. By suitably modulating the experimental condition, the lateral size of the resultant nanometer-sized RGO can be controlled in a desirable range, from 30–100 nm (sample was denoted as nano-RGO) to 2–4 nm (denoted as QD-RGO). For comparison purpose, micrometer-sized RGO sheets (denoted as micro-RGO) were also coupled with CdSe nanocrystals for photoelectrochemical tests. Due to the significant zigzag edge effect, nano-RGO and QD-RGO possessed well-defined band structure that enabled efficient light absorption and distinctive photoluminescence emission. For nano-RGO and QD-RGO, they can act as an effective hole acceptor for CdSe due to their higher highest occupied molecular orbital (HOMO) level (+1.15 V vs. NHE) than the valence band level of CdSe (+1.70 V vs. NHE). With the staggered band alignment, CdSe/nano-RGO and CdSe/QD-RGO nanoheterostructures exhibited remarkably enhanced charge separation for increasing the performance in photoelectrochemical hydrogen production. As to the micro-RGO, the metallic conductive nature made it susceptible to accepting photoexcited electrons from CdSe, which also caused effective charge separation to benefit the photoelectrochemical performance. Among the three CdSe/RGO samples tested, CdSe/QD-RGO achieved the highest photocurrent generation in the photoelectrochemical cell, exceeding 5 times the value of pure CdSe. The incident photon-to-electron conversion efficiency (IPCE) spectra suggested that the significantly enhanced photoactivity of CdSe/QD-RGO was due to the pronounced charge separation as well as the improved light harvesting, as a result of the type-II vectorial charge transfer scenario. Furthermore, no appreciable decay of photocurrent was found for CdSe/QD-RGO after continuously used in the photoelectrochemical cell for over 2 h, revealing its substantially high stability during the water reduction process.

2. Experimental

2.1. Chemicals

All chemicals were analytical grade and used without further purification. Special attention should be paid when dealing with the hazardous Cd source.

2.2. Synthesis of CdSe nanocrystals

CdSe nanocrystals were synthesized with a cysteine-assisted aqueous synthetic method [39]. In the typical procedure, an aqueous solution containing CdSO₄ (2.0 mL, 0.15 M) and L-cysteine (2.6 mL, 1.0 M) was first prepared in a vial, and the pH was adjusted to 10.0 using 1.0 M NaOH. The mixed solution was then diluted to 200 mL with deionized water, followed by the dropwise addition of Na₂SeSO₃ solution (0.75 mL, 0.1 M). The reaction solution was stirred at room temperature for 1 h, producing a stable, yellow dispersion of CdSe nanocrystals. These cysteine-capped CdSe colloids were then allowed to stand for later use.

2.3. Synthesis of micrometer-sized RGO

In this work, GO sheets were hydrothermally treated to produce RGO, an ideal substitute for graphene. GO sheets were obtained from graphite powder by using the Hummers' method [40]. A desirable amount of GO (25 mg) was then dispersed in deionized water (50 mL), and the pH was adjusted to 7.0 using 0.1 M NaOH. Afterwards, the GO suspension was transferred to a Teflon-lined autoclave (100 mL in capacity) and heated at 200 °C for 24 h. After cooling to room temperature, the resultant black precipitate (micrometer-sized RGO, denoted as micro-RGO) was collected by suction filtration and dried in vacuum for later use.

2.4. Synthesis of nanometer-sized RGO

Hydrothermal cutting approach was employed to break the micro-RGO sheets into nanometer-sized RGO pieces [38]. The approach involved the acid oxidation treatment and the hydrothermal deoxidation process. By adjusting the acid treatment time, the lateral size of the resultant ultra-small RGO can be controlled in two different ranges, 30–100 nm and 2–4 nm; the sample was respectively denoted as nano-RGO and QD-RGO. In the typical procedure, GO sheets from Hummers' method (50 mg) were sonicated in a mixed solution of concentrated H₂SO₄ (75 mL) and HNO₃ (25 mL). After refluxed at 100 °C for 8 h, the mixed solution was filtered through a 0.22-μm microporous membrane to remove the acids. The brown filtrate was then transferred to a Teflon-lined autoclave (100 mL in capacity) and heated at 200 °C for 24 h. After cooling to room temperature, the resultant brown suspension (nano-RGO) was collected by centrifugation and re-dispersed in deionized water for later use. To obtain QD-RGO, the same procedure mentioned above was used except that the refluxing time during acid treatment was prolonged to 24 h. The resultant hydrothermally treated brown suspension was further purified in a dialysis bag for 3 days, producing highly stable QD-RGO suspension.

2.5. Preparation of CdSe/RGO nanoheterostructures

The coupling of RGO with CdSe nanocrystals was achieved by using chitosan as the linker molecule [37]. First, RGO (micro-RGO, nano-RGO or QD-RGO, 2.0 mg) was dispersed in the chitosan solution (0.50 wt%, 4.0 mL) and the pH was adjusted to 4.5 using 0.1 M HCl. This process would result in the formation of RGO–chitosan composite. Subsequently, a given concentration of CdSe nanocrystal suspension (9.0 mmol, 8.0 mL) was added to the RGO–chitosan

Table 1
Kinetic analysis of emission decay for pure CdSe and the three CdSe/RGO samples.

	A_1 (%)	τ_1 (ns)	A_2 (%)	τ_2 (ns)	χ^2	k_{CT} (s ⁻¹)
Pure CdSe	37.3	42.56	62.7	5.64	1.13	–
CdSe/micro-RGO	21.6	8.93	78.4	1.69	1.04	0.41×10^9
CdSe/nano-RGO	10.8	5.56	89.2	0.74	1.27	1.17×10^9
CdSe/QD-RGO	11.9	5.32	88.1	0.65	1.09	1.36×10^9

solution under ultrasonication, which allowed for the chemical adsorption of CdSe nanocrystals onto the RGO surface. The products (CdSe/micro-RGO, CdSe/nano-RGO or CdSe/QD-RGO) were collected by centrifugation and dried in vacuum for later use. The content of RGO in the three CdSe/RGO samples was commensurate, around 50 wt%.

2.6. Photoluminescence lifetime measurement

Time-resolved photoluminescence (PL) spectra were measured using a home-built single photon counting system (Horiba Jobin Yvon) which delivers an instrument response function down to 25 ps full width at half-maximum (FWHM). A GaN diode laser ($\lambda = 375$ nm) was used as the excitation source. The signals collected at the excitonic emission of CdSe ($\lambda = 530$ nm) were dispersed with a grating spectrometer, detected by a high-speed photomultiplier tube, and then correlated using a single photon counting card. Upon laser excitation, pronounced charge separation occurred at the interface of the three CdSe/RGO samples, which led to a significant quenching on the emission of CdSe. By comparing the emission decay profiles between CdSe and CdSe/RGO, the interfacial charge transfer event can be quantitatively deduced. The emission decay data were fitted with a biexponential kinetics model which generates two lifetime values, τ_1 and τ_2 , and the corresponding amplitudes, A_1 and A_2 [41,42]. All the fitting results were summarized in Table 1.

2.7. Photoelectrochemical measurement

The photoelectrochemical measurement was conducted in a three-electrode cell which consisted of Pt counter electrode, Ag/AgCl reference electrode and 0.1 M Na₂S/Na₂SO₃ electrolyte. Note that Na₂S/Na₂SO₃ was used as the hole scavenger for the anode to ensure the efficient hydrogen production at the cathode [43]. The photoanode was prepared by dripping sample suspension (100 μ L, 1.0 mg/mL) on the indium tin oxide (ITO) substrate (2.0 cm \times 2.0 cm). After completely dried, the substrate was inserted in the three-electrode cell for measurement. The photoelectrochemical data were collected in an electrochemical station under visible light illumination. The light source was a xenon lamp (500 W, with a light intensity of 100 mW/cm²) collocated with a band pass filter (with the band width of 400–700 nm). The irradiation area on the tested electrode was around 0.785 cm². The incident-photon-to-current-conversion-efficiency (IPCE) spectra were measured under illumination of monochromatic light from the xenon lamp coupled with a monochromator.

2.8. Characterizations

The morphology and dimensions of the samples were examined with a high-resolution transmission electron microscope (HRTEM, JEOL, JEM-3000) operated at 300 kV. The crystallographic structure of the samples was investigated with X-ray diffraction (XRD, Bruker, D2 phaser). The elemental analysis was conducted with the energy dispersive X-ray spectrometry (EDS), an accessory of TEM (JEM-3000). UV-visible absorption spectra and steady-state PL spectra were obtained at room temperature with a Hitachi

U-3900H spectrophotometer and a Hitachi F-4500, respectively. The cyclic voltammetry (CV) measurement was performed in an electrochemical station which used Pt wire as working electrode, carbon rod as counter electrode, and Ag/AgCl as the reference. Prior to each CV measurement, the working electrode was polished and rinsed with deionized water. The CV profile was recorded in a 0.1 M KCl buffer in the presence of the sample suspension (1 mg/mL). The scan potential ranged from -1.5 V to 1.5 V and the scan rate was set at 100 mV/s. The Brunauer–Emmett–Teller (BET) specific surface areas of the samples were estimated from the N₂ adsorption/desorption analysis.

3. Results and discussion

First, CdSe nanocrystals with a typical size of 2.4 ± 0.6 nm were obtained in an aqueous synthesis which used L-cysteine as the capping molecule [39]. As Fig. 1(a) shows, these cysteine-capped nanocrystals were crystalline with clear lattice fringes that can be assigned to the zinc blende CdSe. On the other hand, nanometer-sized RGO was prepared with the hydrothermal cutting approach [38,44], which involved the acid oxidation treatment on GO sheets and the subsequent hydrothermal deoxidation reaction. By adjusting the acid treatment time, the lateral size of the resultant RGO can be controlled in two different ranges. When the acid treatment time was 8 h, small RGO pieces with the lateral size of 30–100 nm were obtained (nano-RGO). As prolonging the acid treatment time to 24 h, the size of the resultant RGO decreased dramatically to 2–4 nm (QD-RGO). As shown in Fig. 1(b) and (c), both of the nano-RGO and QD-RGO were highly crystalline and exhibited well-resolved lattice fringes. The observed interlayer spacing of 0.21 nm agreed well with the lattice spacing of the in-plane (1 0 0) facet of graphene [31]. These ultrafine RGO structures were then modified with chitosan to enrich their surface functionality [37]. Note that chitosan is a polysaccharide biopolymer that has amino and hydroxyl groups. The modification with chitosan may impart RGO with additional functionalities for subsequent chemical grafting. Here, chitosan modification can facilitate the coupling of RGO with cysteine-capped CdSe nanocrystals because part of the chitosan moieties may bind to the CdSe surface through the amide linkage [45]. This attribute is crucial to attain an intimate contact of RGO with CdSe, which is believed to be important for promoting the interfacial charge transfer. For comparison purpose, micrometer-sized RGO (micro-RGO) was also prepared and modified with chitosan for further coupling with CdSe. Fig. 1(d)–(f) presents the morphology of the three CdSe/RGO nanoheterostructures samples. In Fig. 1(d) and (e), a single sheet of CdSe/micro-RGO and CdSe/nano-RGO was exemplified. Evidently, micro-RGO and nano-RGO were covered by a large quantity of CdSe nanocrystals, demonstrating the success of the chitosan modification conception in assembling RGO and CdSe. As to the CdSe/QD-RGO sample, it appeared as the heterodimer structures with well-defined lattice fringes that can be respectively assigned to CdSe and RGO. Such a structural feature suggested the effective linking of CdSe to QD-RGO, which can be confirmed by the significant electronic interaction between the two constituents, as will be discussed later in the PL spectroscopy. The composition of CdSe in the three CdSe/RGO samples was further confirmed by XRD analysis and TEM-EDS mapping results (Figs. S1 and S2, see Supplementary data).

The optical properties of the samples were studied with absorption and PL spectroscopy. Fig. 2(a) and (b) first shows the UV–vis absorption and PL spectra recorded on the aqueous dispersions of the three pristine RGO. For micro-RGO, a strong $\pi \rightarrow \pi^*$ absorption edge extending to the middle UV region was noticed [38]. No detectable PL can be found in the wavelength range of 400–600 nm, which is expectable because the metallic, large-sized micro-RGO

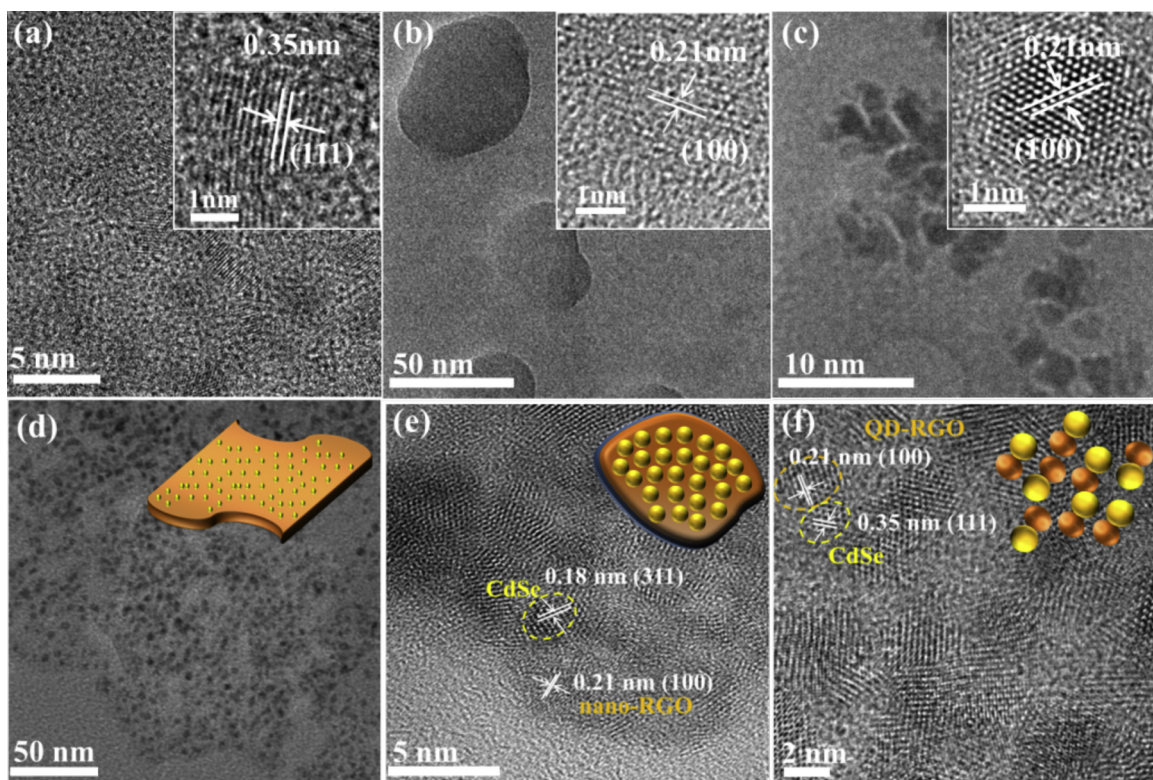


Fig. 1. TEM images of (a) pure CdSe, (b) nano-RGO, (c) QD-RGO, (d) CdSe/micro-RGO, (e) CdSe/nano-RGO and (f) CdSe/QD-RGO. Insets in (a)–(c) show the corresponding HRTEM images. Insets in (d)–(f) depict the structural feature of the samples.

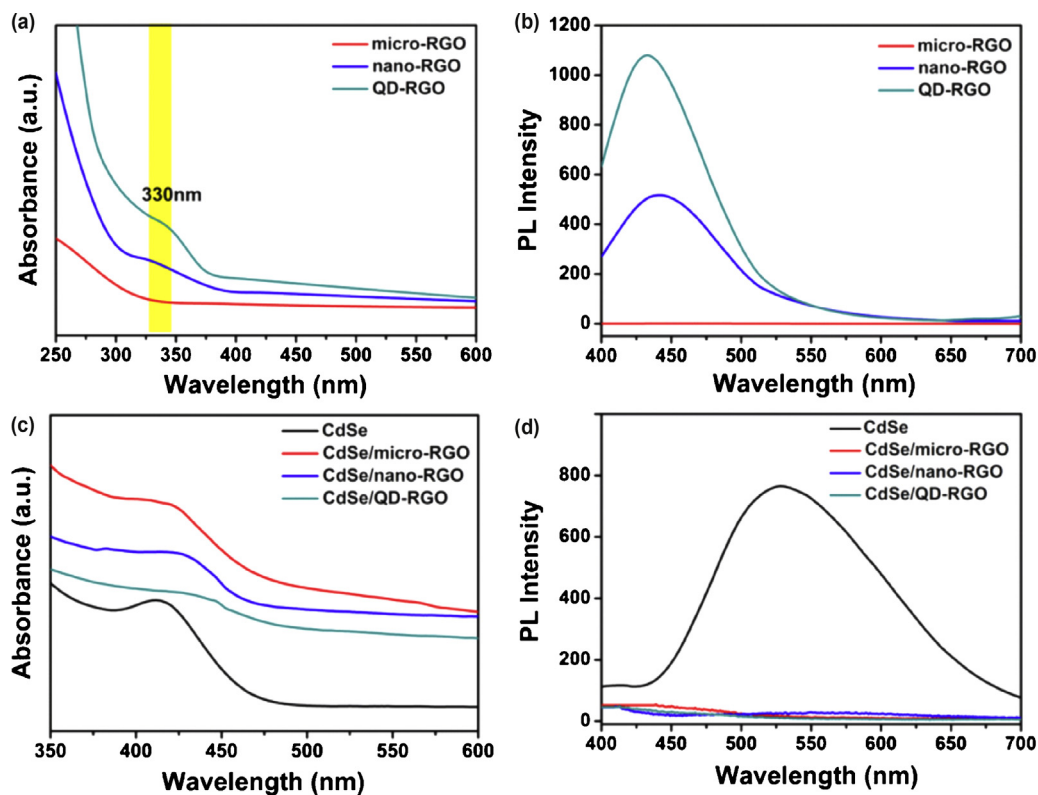


Fig. 2. (a) UV-vis absorption and (b) steady-state PL spectra for micro-RGO, nano-RGO, and QD-RGO. (c) UV-vis absorption and (d) steady-state PL spectra for pure CdSe, CdSe/micro-RGO, CdSe/nano-RGO and CdSe/QD-RGO. The excitation wavelength of PL was 335 nm.

was unable to emit efficiently [46]. On the other hand, an unambiguous absorption shoulder at 330 nm can be identified for nano-RGO and QD-RGO, fairly close to the reported values of graphene QDs [30,38,47,48]. Note that the edges of the chemically derived graphene (e.g. RGO) consist of zigzag and armchair sites. The zigzag sites are carbene-like and have a triplet ground state described as $\sigma^1\pi^1$ [38]. By supplying appropriate excitation energies, the localized electrons at σ and π orbitals (HOMO) can be excited to the lowest unoccupied molecular orbital (LUMO). Because of the small lateral size, nanometer-sized RGO had a large number of zigzag sites and thereby possessed the HOMO–LUMO energy gap. For the present nano-RGO and QD-RGO, the observed absorption at 330 nm can be regarded as the electronic transitions from the π orbital to the LUMO [38]. In contrast to the micro-RGO, nano-RGO and QD-RGO both emitted excitation-dependent PL with the strongest peak recorded at around 440 nm (Fig. S3, see Supplementary data). In Fig. 2(b), the FWHM of the recorded PL was about 96 nm, approximate to those reported for graphene QDs [38]. This blue emission can be ascribed to the zigzag edge effect of ultrafine graphene, which described the radiative deactivation of excited electrons from the LUMO to the HOMO [38,48,49]. The observations from absorption spectra and PL characterizations suggested that unlike micro-RGO, nano-RGO and QD-RGO had a well-defined HOMO–LUMO energy gap that enabled efficient light absorption and distinctive PL emission. This unique optical feature may diversify the applicability of nano-RGO and QD-RGO especially in the semiconductor-based photocatalysis as they could contribute to the overall photon harvesting as well as mediate the interfacial charge transfer.

Fig. 2(c) and (d) presents the absorption and emission spectra for the three CdSe/RGO samples. The spectra of pure CdSe nanocrystals were also collected for comparison. As noticed in Fig. 2(c), pure CdSe nanocrystals showed an absorption onset at 462 nm, corresponding to an optical bandgap of 2.68 eV. This value was in conformity with the calculated bandgap for 2.0 nm sized CdSe [50]. All the CdSe/RGO samples were characterized by pronounced light absorption in the visible region, which can be attributed to the bandgap absorption of the composed CdSe. In particular, CdSe/micro-RGO showed a perceptible redshift in the absorption onset with respect to pure CdSe. Such a redshift can be ascribed to the agglomeration of CdSe on the relatively large micro-RGO [51]. In Fig. 2(d), the PL spectrum of pure CdSe nanocrystals exhibited a major emission band at 550 nm, which was assigned to the excitonic band edge emission of CdSe. The apparent Stokes shift of about 80 nm presumably resulted from the band edge multiplicity caused by the small size of CdSe [52]. Compared with pure CdSe and pristine RGO, the three CdSe/RGO displayed a substantially depressed PL emission in the wavelength range of 400–600 nm, suggesting that charge recombination in CdSe and RGO was greatly retarded upon their combination. This demonstration revealed that effective charge separation can be achieved by combining CdSe with RGO, even with the nanometer-sized RGO, which is very inspirational toward the development of semiconductor/graphene composite photocatalysts.

Time-resolved PL measurements were conducted to explore the charge transfer events within the CdSe/RGO samples. Note that time-resolved PL studies have proven useful for the characterization of charge carrier dynamics because PL is the primary pathway through which the electron-hole pairs recombine and dissipate [53–58]. Fig. 3 compares the time-resolved PL spectra of pure CdSe and the three CdSe/RGO samples. Notably, the three CdSe/RGO exhibited dissimilar PL decay profiles from that of pure CdSe, implying the significant electronic interaction between CdSe and RGO. The spectra in Fig. 3 were fitted with a biexponential function to generate a slow (τ_1) and a fast (τ_2) decay component, which was respectively assigned to radiative and nonradiative

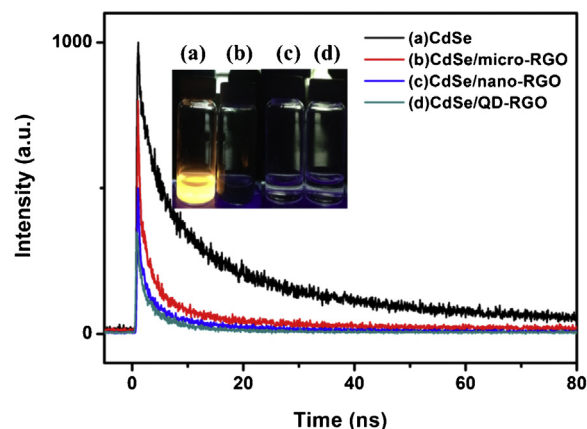


Fig. 3. Time-resolved PL spectra for (a) pure CdSe, (b) CdSe/micro-RGO, (c) CdSe/nano-RGO and (d) CdSe/QD-RGO. Inset shows the colors of the sample suspensions upon irradiation with a UV lamp.

deactivation processes [41,42]. As noted in Table 1, for the three CdSe/RGO samples, the two decay components of CdSe were both shortened upon the RGO coupling. This phenomenon suggested that the three RGO competed with the excited state deactivation of CdSe by providing extra nonradiative pathways for charge carrier transfer, which was accountable for the shortening of PL lifetime and the prevalence of charge separation. Here we assumed that the interfacial charge transfer between CdSe and RGO dictated the emission decay of CdSe/RGO. The charge-transfer rate constant (k_{CT}) at the interface of CdSe/RGO can then be calculated by the expression $k_{CT}(\text{CdSe} \rightarrow \text{RGO}) = (1/\tau_2 - 1/\tau_1)(\text{CdSe/RGO}) - (1/\tau_2)(\text{CdSe})$ [59]. The estimated k_{CT} value was $0.41 \times 10^9 \text{ s}^{-1}$, $1.17 \times 10^9 \text{ s}^{-1}$ and $1.36 \times 10^9 \text{ s}^{-1}$ for CdSe/micro-RGO, CdSe/nano-RGO and CdSe/QD-RGO, respectively. Evidently, CdSe/nano-RGO and CdSe/QD-RGO attained a higher k_{CT} than CdSe/micro-RGO did, illustrating that the two nanometer-sized RGO surpassed micro-RGO in enhancing the charge separation efficiency of CdSe. The considerably high k_{CT} value observed for CdSe/QD-RGO also verified that the structural coupling between CdSe and QD-RGO was effective although it was improbable to be identified in Fig. 1(f). Since the content of RGO for the three CdSe/RGO samples was commensurate, the higher k_{CT} of CdSe/nano-RGO and CdSe/QD-RGO was unlikely to derive from the quantitative effect of RGO [59], but rather was possibly associated with the unique optical feature of the nanometer-sized RGO. For CdSe/micro-RGO, the highly conductive micro-RGO would attract the photoexcited electrons from CdSe, simultaneously leaving photogenerated holes at CdSe to achieve charge separation. This unidirectional electron transfer mechanism has been adopted in most semiconductor/graphene composite systems. Because the present nano-RGO and QD-RGO exhibited distinct optical properties from micro-RGO, the mechanism behind the pronounced charge separation of CdSe/nano-RGO and CdSe/QD-RGO should be essentially different.

In order to elucidate the role of nano-RGO and QD-RGO in mediating the charge transfer of CdSe, we performed CV measurement to delineate the band structure of the samples [51]. Fig. 4 shows the CV profiles recorded on the sample dispersions in KCl buffer. For pure CdSe, a cathodic peak was recorded at -1.08 V (vs. Ag/AgCl). As to the nano-RGO and QD-RGO, a broad but definite anodic peak can be identified at around $+0.95 \text{ V}$ (vs. Ag/AgCl). Note that the anodic and cathodic signals during CV measurement arise from the effective charge transfer across the sample/electrolyte interface through the HOMO (equivalent to the valence band) and LUMO (equivalent to the conduction band) edges of the sample, respectively. The recorded anodic and cathodic peak potentials can thus be

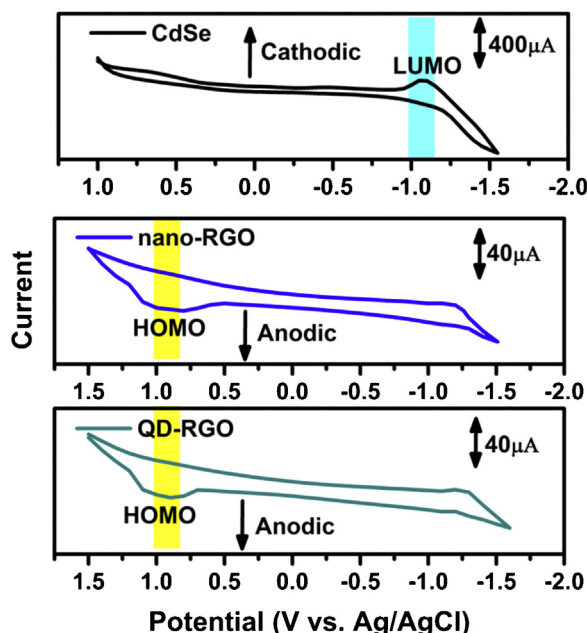


Fig. 4. CV profiles recorded on pure CdSe, nano-RGO and QD-RGO.

respectively referred to the HOMO and LUMO levels of the tested sample. According to the CV results, we obtained the conduction band level of -0.88 V (vs. NHE) for pure CdSe, and the HOMO level of $+1.15$ V (vs. NHE) for both nano-RGO and QD-RGO. The valence band level of CdSe can be further calculated by subtracting the optical bandgap value (2.58 eV, as derived from Fig. 2(c)) from the respective conduction band level, which gives $+1.70$ V (vs. NHE). Similarly, by taking the absorption shoulder of 330 nm as the gap energy (3.75 eV, as derived from Fig. 2(a)), the LUMO level of nano-RGO and QD-RGO can be computed to be -2.60 V (vs. NHE). Based on the obtained band edge levels, we proposed a type-II staggered band alignment model [60] to account for the interfacial charge transfer for CdSe/nano-RGO and CdSe/QD-RGO. Taking CdSe/QD-RGO as the example, under light illumination the photoexcited electrons of QD-RGO would preferentially transfer to CdSe due to the higher LUMO level of QD-RGO (-2.60 V vs. NHE) than the conduction band level of CdSe (-0.88 V vs. NHE); meanwhile, the photogenerated holes at CdSe ($+1.70$ V vs. NHE) could be readily passed to the QD-RGO domain because of the higher HOMO level of QD-RGO ($+1.15$ V vs. NHE). This vectorial charge transfer may induce a built-in electric field at the CdSe/QD-RGO interface, which further facilitated the transportation of electrons and holes in opposite directions [60]. Consequently, remarkably enhanced charge separation was attained in CdSe/nano-RGO and CdSe/QD-RGO, which could be accountable for their considerably higher k_{CT} values as derived in the time-resolved PL study.

The type-II vectorial charge transfer model of CdSe/nano-RGO and CdSe/QD-RGO was contrasted to the unidirectional electron transfer mechanism of CdSe/micro-RGO in terms of the scenario of charge transfer. Specifically, the situation that the photogenerated holes were mostly localized at the nano-RGO and QD-RGO and did not accumulate in CdSe has significant implications in the photocatalytic applications because the typical photocorrosion problem of CdSe may be properly addressed. To compare the performance of the three CdSe/RGO samples in the practical photocatalytic process, photoelectrochemical studies were carried out by employing them as photoanodes for photoelectrochemical hydrogen production. Fig. 5 shows the linear sweep voltammograms recorded from pure CdSe and the three CdSe/RGO samples in the dark and under visible light illumination. Several important features can be observed.

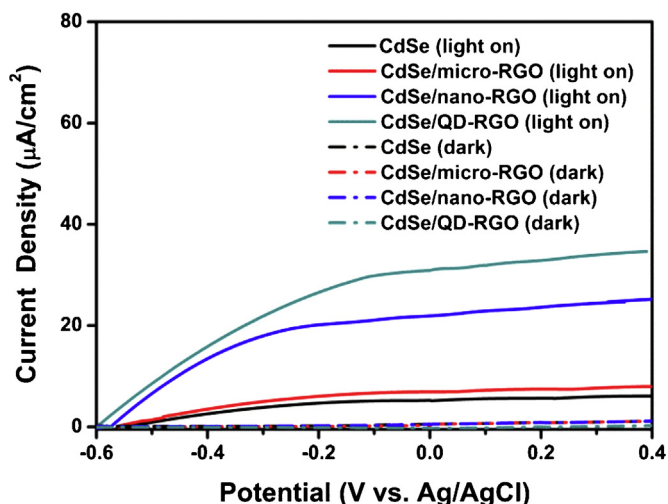


Fig. 5. Linear sweep voltammograms for different samples recorded in the dark and under visible light illumination.

First, all the samples showed negligible dark current density in the entire scanning region, which can obviate the possibility of erroneous interpretation on their photoresponse behaviors. Second, as compared to pure CdSe, the three CdSe/RGO samples all exhibited higher photocurrent generation, manifesting the positive role of the three RGO in enhancing the photoactivity of CdSe toward photoelectrochemical hydrogen production. Third, among the three CdSe/RGO samples examined, CdSe/QD-RGO achieved the highest photocurrent generation of $30.9 \mu\text{A}/\text{cm}^2$ at 0 V vs. Ag/AgCl, which exceeded 5 times the value of pure CdSe ($5.2 \mu\text{A}/\text{cm}^2$). In contrast, CdSe/micro-RGO ($6.9 \mu\text{A}/\text{cm}^2$) only attained around 30% photocurrent increase over pure CdSe. This photoactivity difference originated from the fact that QD-RGO surpassed micro-RGO in enhancing the charge separation efficiency of CdSe, as was demonstrated in the time-resolved PL analysis. In addition, the type-II vectorial charge transfer feature also conducted to the substantially higher photocurrent enhancement for CdSe/QD-RGO. In this regard, the photocurrent would be increased due to the efficient hole transfer from CdSe to QD-RGO. Because QD-RGO was of high chemical inertness, the holes transferred to QD-RGO can readily oxidize the sacrificial reagent without deteriorating the structure of QD-RGO. This could assist in maintaining the stability of CdSe/QD-RGO as well as facilitating the interfacial charge transfer, both of which were favorable for photocurrent generation. The above proposition will be later validated by the long-term stability test. It should be mentioned that the three CdSe/RGO samples had comparable BET surface areas: 21.3 , 22.1 and $21.8 \text{ m}^2/\text{g}$ for CdSe/micro-RGO, CdSe/nano-RGO and CdSe/QD-RGO, respectively. This outcome illustrated that the superior photoactivity of CdSe/nano-RGO and CdSe/QD-RGO over CdSe/micro-RGO was not related to the surface area factor, but resulted from the type-II vectorial charge transfer feature. Lastly, the onset potential of pure CdSe was about -0.56 V vs. Ag/AgCl, which shifted to -0.60 V after the QD-RGO coupling. The improved interfacial charge transfer of CdSe/QD-RGO, as a result of the type-II vectorial charge transfer scenario, could be responsible for the observed negative shift of onset potential [61,62].

To further quantify the photoactivity of the samples in the photoelectrochemical hydrogen production, we performed IPCE measurements and explored the photoactive wavelength regime. The IPCE values can be determined from the equation $\text{IPCE} = (1240 I) / (\lambda J_{\text{light}})$, where I is the measured photocurrent density, J_{light} is the measured irradiance at a specific wavelength, and λ is the incident light wavelength. As Fig. 6(a) shows, the three CdSe/RGO samples

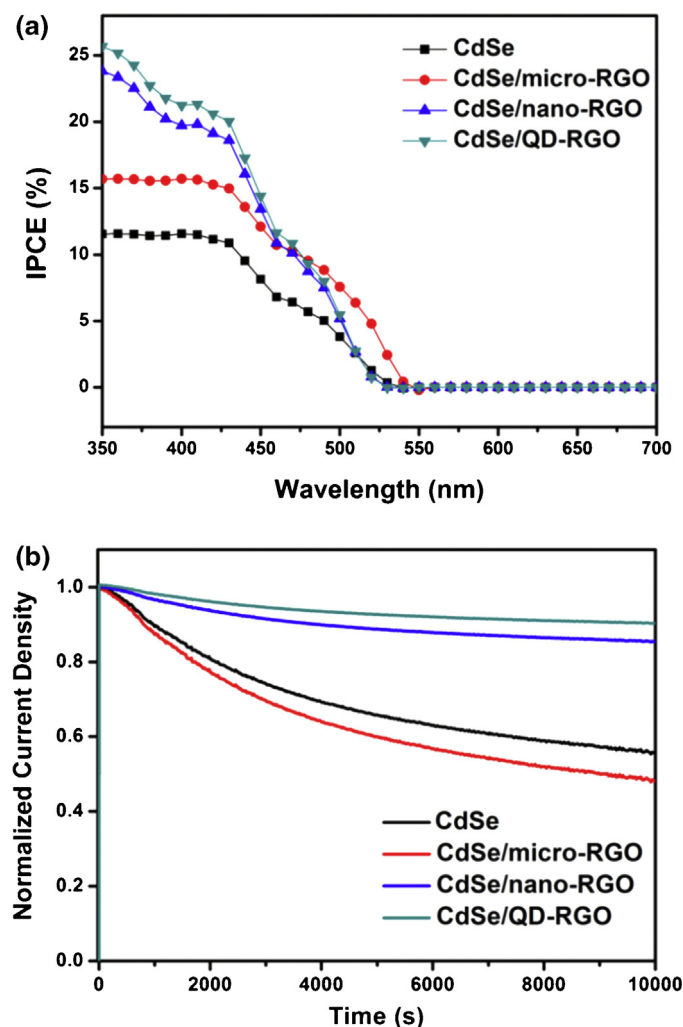


Fig. 6. (a) IPCE plots and (b) amperometric $I-t$ curves for pure CdSe and the three CdSe/RGO samples collected at 0 V vs. Ag/AgCl. In (b), the photocurrent density was shown in normalized value for cross-comparison among samples.

had similar IPCE characteristics to the result of pure CdSe, indicating that the recorded photocurrents were dominated by the photoactivity of the composed CdSe, i.e. the light harvesting of CdSe and the subsequent carrier generation and transfer. In comparison to pure CdSe, the three CdSe/RGO displayed substantially increased IPCE values, with CdSe/QD-RGO having the largest increment, which was consistent with the observations from Fig. 5. Another conspicuous feature is that the IPCE enhancement in the near-UV region (350–400 nm) was particularly pronounced for CdSe/nano-RGO and CdSe/QD-RGO. This wavelength regime was well-matched with the HOMO–LUMO absorption region of nano-RGO and QD-RGO. Therefore, we attributed this feature to the coupling of nano-RGO and QD-RGO, which improved the overall photoconversion efficiency by absorbing additional photons in the UV region. Moreover, as compared to the absorption spectra, an evident redshift of IPCE spectral onset was found for all the samples. This might be due to the inevitable aggregation of CdSe nanocrystals during the electrode preparation process. Since the large-sized, 2D micro-RGO sheets were prone to restacking on the ITO surface, aggregation of CdSe was particularly prevalent in CdSe/micro-RGO electrode, as can be identified from the much larger extent of the absorption redshift (Fig. S4, see Supplementary data). Such a significant aggregation of CdSe for CdSe/micro-RGO further led to the noticeable photoactivity observed at 500–550 nm. Furthermore, the

amperometric $I-t$ study was performed to evaluate the stability of the samples in the photoelectrochemical cell. As illustrated in Fig. 6(b), upon continuous illumination for over 2 h, the photocurrent density of pure CdSe and CdSe/micro-RGO greatly declined by 41.5 and 42.6%, respectively, revealing that severe photocorrosion took place on CdSe even though the hole scavenger was employed. On the contrary, the photocurrent value of CdSe/nano-RGO and CdSe/QD-RGO was quite stable, which respectively dropped 14.2% and 7.4% during the same illumination period. Such a high stability presumably derived from the fact that nano-RGO and QD-RGO could ease the hole accumulation on CdSe by mediating the hole transfer.

4. Conclusions

In conclusion, we have successfully developed CdSe/QD-RGO nanoheterostructures as the photoanode for remarkable photoelectrochemical hydrogen production. Due to the significant zigzag edge effect, QD-RGO possessed a well-defined HOMO–LUMO bandgap which collocated with the band edge of CdSe in a type-II staggered band offset. Compared to pure CdSe and CdSe/micro-RGO, CdSe/QD-RGO exhibited substantially higher photocurrent generation under visible light illumination, demonstrating that the coupling of QD-RGO was more effective than the coupling of micro-RGO in increasing the photoelectrochemical performance of CdSe. The results of IPCE measurements suggested that the photoactivity enhancement of CdSe/QD-RGO was attributed to the type-II vectorial charge transfer feature, which achieved pronounced charge carrier separation as well as improved the overall light harvesting. Furthermore, CdSe/RGO retained comparable photoactivity after continuously used in the photoelectrochemical cell for over 2 h, revealing its stability and applicability in the long-term course of photocatalysis. The type-II vectorial charge transfer scenario makes the present CdSe/QD-RGO nanoheterostructures especially promising in the practical photooxidation applications, such as photocatalytic oxygen evolution and oxidative organic transformation. The current study is expected to open up a new avenue toward the design of graphene QDs-based nanoheterostructures in technologically important optoelectronics fields, where the advantageous characteristics of graphene QDs, i.e. the light harvesting capability and high chemical inertness, can be fully exploited.

Acknowledgement

This work was financially supported by the Ministry of Science and Technology of ROC (Taiwan) under grants NSC-102-2113-M-009-005-MY2 and NSC-102-3113-P-009-002.

Appendix A. Supplementary data

Supplementary material related to this article can be found, in the online version, at <http://dx.doi.org/10.1016/j.apcatb.2014.09.034>.

References

- [1] K.S. Novoselov, A.K. Geim, S.V. Morozov, D. Jiang, Y. Zhang, S.V. Dubonos, I.V. Grigorieva, A.A. Firsov, *Science* 306 (2004) 666–669.
- [2] K.S. Novoselov, D. Jiang, F. Schedin, T.J. Booth, V.V. Khotkevich, S.V. Morozov, A.K. Geim, *Proc. Natl. Acad. Sci. U. S. A.* 102 (2005) 10451–10453.
- [3] A.K. Geim, K.S. Novoselov, *Nat. Mater.* 6 (2007) 183–191.
- [4] H. Wang, Y. Liang, T. Mirfakhrai, Z. Chen, H.S. Casalongue, H. Dai, *Nano Res.* 4 (2011) 729–736.
- [5] F. Bonaccorso, Z. Sun, T. Hasan, A.C. Ferrari, *Nat. Photonics* 4 (2010) 611–622.
- [6] X. Song, M. Oksanen, M.A. Sillanpää, H.G. Craighead, J.M. Parpia, P.J. Hakonen, *Nano Lett.* 12 (2012) 198–202.
- [7] F. Yavari, N. Koratkar, *J. Phys. Chem. Lett.* 3 (2012) 1746–1753.
- [8] W. Yuan, G. Shi, *J. Mater. Chem. A* 1 (2013) 10078–10091.

- [9] N. Zhang, Y. Zhang, Y.J. Xu, *Nanoscale* 4 (2012) 5792–5813.
- [10] Q. Xiang, J. Yu, M. Jaroniec, *Chem. Soc. Rev.* 41 (2012) 782–796.
- [11] R.C. Pawar, C.S. Lee, *Appl. Catal. B: Environ.* 144 (2014) 57–65.
- [12] Y. Houa, X. Lia, Q. Zhaoa, G. Chen, *Appl. Catal. B: Environ.* 142–143 (2013) 80–88.
- [13] X. Bai, L. Wang, R. Zong, Y. Lv, Y. Sun, Y. Zhu, *Langmuir* 29 (2013) 3097–3105.
- [14] G.K. Pradhan, D.K. Padhi, K.M. Parida, *ACS Appl. Mater. Interfaces* 5 (2013) 9101–9110.
- [15] B. Qiu, M. Xing, J. Zhang, *J. Am. Chem. Soc.* 136 (2014) 5852–5855.
- [16] J.L. Xie, C.X. Guo, C.M. Li, *Energy Environ. Sci.* 7 (2014) 2559–2579.
- [17] A.H. Castro Neto, F. Guinea, N.M.R. Peres, K.S. Novoselov, A.K. Geim, *Rev. Mod. Phys.* 81 (2009) 109–162.
- [18] K.S. Novoselov, A.K. Geim, S.V. Morozov, D. Jiang, M.I. Katsnelson, I.V. Grigorieva, S.V. Dubonos, A.A. Firsov, *Nature* 438 (2005) 197–200.
- [19] Q. Yan, B. Huang, J. Yu, F. Zheng, J. Zang, J. Wu, B.L. Gu, F. Liu, W. Duan, *Nano Lett.* 7 (2007) 1469–1473.
- [20] X. Wang, X. Li, L. Zhang, Y. Yoon, P.K. Weber, H. Wang, J. Guo, H. Dai, *Science* 324 (2009) 768–771.
- [21] A.J. Samuels, J.D. Carey, *ACS Nano* 7 (2013) 2790–2799.
- [22] M.Y. Han, B.O. Zylmaz, Y. Zhang, P. Kim, *Phys. Rev. Lett.* 98 (2007) 206805.
- [23] S.Y. Zhou, G.H. Gweon, A.V. Fedorov, P.N. First, W.A.D. Heer, D.H. Lee, F. Guinea, H.C. Neto, A. Lanzara, *Nat. Mater.* 6 (2007) 770–774.
- [24] X. Li, X. Wang, L. Zhang, S. Lee, H. Dai, *Science* 319 (2008) 1229–1231.
- [25] M. Dvorak, W. Oswald, Z. Wu, *Sci. Rep.* 3 (2013) 2289.
- [26] H. Sun, L. Wu, N. Gao, J. Ren, X. Qu, *ACS Appl. Mater. Interfaces* 5 (2013) 1174–1179.
- [27] J.K. Kim, M.J. Park, S.J. Kim, D.H. Wang, S.P. Cho, S. Bae, J.H. Park, B.H. Hong, *ACS Nano* 7 (2013) 7207–7212.
- [28] Y. Li, Y. Hu, Y. Zhao, G. Shi, L. Deng, Y. Hou, L. Qu, *Adv. Mater.* 23 (2011) 776–780.
- [29] V. Gupta, N. Chaudhary, R. Srivastava, G.D. Sharma, R. Bhardwaj, S. Chand, *J. Am. Chem. Soc.* 133 (2011) 9960–9963.
- [30] S. Zhu, J. Zhang, C. Qiao, S. Tang, Y. Li, W. Yuan, B. Li, L. Tian, F. Liu, R. Hu, H. Gao, H. Wei, H. Zhang, H. Sun, B. Yang, *Chem. Commun.* 47 (2011) 6858–6860.
- [31] W. Kwon, Y.H. Kim, C.L. Lee, M. Lee, H.C. Choi, T.W. Lee, S.W. Rhee, *Nano Lett.* 14 (2014) 1306–1311.
- [32] X. Yan, X. Cui, B. Li, L. Li, *Nano Lett.* 10 (2010) 1869–1873.
- [33] X. Sun, Z. Liu, K. Welscher, J.T. Robinson, A. Goodwin, S. Zaric, H. Dai, *Nano Res.* 1 (2008) 203–212.
- [34] C.X. Guo, Y. Dong, H.B. Yang, C.M. Li, *Adv. Energy Mater.* 3 (2013) 997–1003.
- [35] Y. Yu, J. Ren, M. Meng, *Int. J. Hydrog. Energy* 38 (2013) 12266–12272.
- [36] K. Chang, Z. Mei, T. Wang, Q. Kang, S. Ouyang, J. Ye, *ACS Nano* 8 (2014) 7078–7087.
- [37] T. Wang, S. Zhang, C. Mao, J. Song, H. Niu, B. Jin, Y. Tian, *Biosens. Bioelectron.* 31 (2012) 369–375.
- [38] D. Pan, J. Zhang, Z. Li, M. Wu, *Adv. Mater.* 22 (2010) 734–738.
- [39] Y.S. Park, A. Dmytruk, I. Dmitruk, A. Kasuya, M. Takeda, N. Ohuchi, Y. Okamoto, N. Kaji, M. Tokeshi, Y. Baba, *ACS Nano* 4 (2010) 121–128.
- [40] X. Zhou, X. Huang, X. Qi, S. Wu, C. Xue, F.Y.C. Boey, Q. Yan, P. Chen, H. Zhang, *J. Phys. Chem. C* 113 (2009) 10842–10846.
- [41] M. Furis, J.A. Hollingsworth, V.I. Klimov, S.A. Crooker, *J. Phys. Chem. B* 109 (2005) 15332–15338.
- [42] J. Zhang, X. Zhang, *J. Phys. Chem. C* 113 (2009) 9512–9515.
- [43] J. Hensel, G. Wang, Y. Li, J.Z. Zhang, *Nano Lett.* 10 (2010) 478–483.
- [44] Z. Li, W. Zhang, Y. Luo, J. Yang, J.G. Hou, *J. Am. Chem. Soc.* 131 (2009) 6320–6321.
- [45] Y. Ding, G. Gu, X. Xia, Q. Huoc, *J. Mater. Chem.* 19 (2009) 795–799.
- [46] K.J. Jeon, Z. Lee, E. Pollak, L. Moreschini, A. Bostwick, C. Park, R. Mendelsberg, V. Radmilovic, R. Kostecki, T.J. Richardson, E. Rotenberg, *ACS Nano* 5 (2011) 1042–1046.
- [47] S. Zhu, J. Zhang, X. Liu, B. Li, X. Wang, S. Tang, Q. Meng, Y. Li, C. Shi, R. Hu, B. Yang, *RSC Adv.* 2 (2012) 2717–2720.
- [48] J. Shen, Y. Zhu, C. Chen, X. Yang, C. Li, *Chem. Commun.* 47 (2011) 2580–2582.
- [49] L.R. Radovic, B. Bockrath, *J. Am. Chem. Soc.* 127 (2005) 5917–5927.
- [50] J. Jasieniak, M. Califano, S.E. Watkins, *ACS Nano* 5 (2011) 5888–5902.
- [51] G.B. Markad, S. Battu, S. Kapoor, S.K. Haram, *J. Phys. Chem. C* 117 (2013) 20944–20950.
- [52] A. Bagga, P.K. Chattopadhyay, S. Ghosh, *Phys. Rev. B* 74 (2006) 035341.
- [53] Y.H. Lu, W.H. Lin, C.Y. Yao, Y.H. Chiu, Y.C. Pu, M.H. Lee, Y.C. Tseng, Y.J. Hsu, *Nanoscale* 6 (2014) 8796–8803.
- [54] W.H. Lin, T.F.M. Chang, Y.H. Lu, T. Sato, M. Sone, K.H. Wei, Y.J. Hsu, *J. Phys. Chem. C* 117 (2013) 25596–25603.
- [55] Y.F. Lin, Y.J. Hsu, *Appl. Catal. B: Environ.* 130–131 (2013) 93–98.
- [56] M.Y. Chen, Y.J. Hsu, *Nanoscale* 5 (2013) 363–368.
- [57] Y.C. Chen, Y.C. Pu, Y.J. Hsu, *J. Phys. Chem. C* 116 (2012) 2967–2975.
- [58] T.T. Yang, W.T. Chen, Y.J. Hsu, K.H. Wei, T.Y. Lin, T.W. Lin, *J. Phys. Chem. C* 114 (2010) 11414–11420.
- [59] I.V. Lightcap, P.V. Kamat, *J. Am. Chem. Soc.* 134 (2012) 7109–7116.
- [60] Y. Wang, Q. Wang, X. Zhan, F. Wang, M. Safdar, J. He, *Nanoscale* 5 (2013) 8326–8339.
- [61] Y.X. Yu, W.X. Ouyang, Z.T. Liao, B.B. Du, W.D. Zhang, *ACS Appl. Mater. Interfaces* 6 (2014) 8467–8474.
- [62] K.H. Yoon, D.K. Seo, Y.S. Cho, D.H. Kang, *J. Appl. Phys.* 84 (1998) 3954.